PNAS RESEARCH ARTICLE | PHYSICS

High-performance seawater oxidation by a homogeneous multimetallic layered double hydroxide electrocatalyst

Luo Yu[a,b,c], Jiayong Xiao[d], Chuqiang Huang[d], Jianqing Zhou[e], Ming Qiu[d], Ying Yu[d], Zhifeng Ren[b,c,1], Ching-Wu Chu[b,c,1], and Jimmy C. Yu[a,1]

Contributed by Ching-Wu Chu; received February 9, 2022; accepted March 22, 2022; reviewed by Jinhua Chen, Yi Du, Gang Wu, and Zhichuan J. Xu

Seawater electrolysis is an intriguing technology for sustainable hydrogen production that will not exacerbate the global shortage of freshwater or increase carbon emissions. However, due to the undesirable anodic chlorine evolution reaction and the strong corrosiveness of seawater, this technology is significantly hindered by a lack of robust oxygen evolution reaction (OER) electrocatalysts that exhibit high activity, high selectivity, and good stability. Here, we demonstrate a homogeneous multimetallic catalyst consisting of Ni and Fe coincorporated into CuCo layered double hydroxide (denoted as NiFe-CuCo LDH) that serves as an active and durable OER electrode for high-performance seawater electrolysis. With abundant exposed multimetal sites and well-defined micronanostructures, the NiFe-CuCo LDH catalyst requires overpotentials of only 259, 278, and 283 mV to yield current densities of 100, 300, and 500 mA cm^{-2}, respectively, in 6 M KOH seawater electrolyte. Moreover, it exhibits very high OER selectivity (Faradaic efficiency of 97.4% for O_2 at 500 mA cm^{-2}) and superior durability during operation, working stably under a large current density of 500 mA cm^{-2} for up to 500 h in 6 M KOH seawater electrolyte. This multimetallic electrocatalyst is one of the best performing ones among all reported transition-metal-based OER electrocatalysts in alkaline seawater electrolyte, which boosts the development of seawater electrolysis technology.

seawater electrolysis | OER | high performance | multimetallic electrocatalyst | layered double hydroxide

Significance

Seawater is one of the most abundant resources on Earth. Direct electrolysis of seawater is a transformative technology for sustainable hydrogen production without causing freshwater scarcity. However, this technology is severely impeded by a lack of robust and active oxygen evolution reaction (OER) electrocatalysts. Here, we report a highly efficient OER electrocatalyst composed of multimetallic layered double hydroxides, which affords superior catalytic performance and long-term durability for high-performance seawater electrolysis. To the best of our knowledge, this catalyst is among the most active for OER and it advances the development of seawater electrolysis technology.

Electrochemical water splitting has been recognized as one of the most promising approaches to produce hydrogen (H_2) energy sustainably and without any carbon emissions (1–5). There has been great progress in the development of this technology in recent years based on the discovery of many efficient and low-cost electrocatalysts (6–9). However, all of these electrocatalysts are operated in aqueous electrolytes prepared using high-purity freshwater, which would exacerbate the global freshwater shortage if water electrolysis were commercialized on a large scale (10). Considering the abundance and accessibility of earth's seawater resources, extracting hydrogen via seawater electrolysis is a much more significant technology, especially for the arid zones located near ocean coastlines (11–13). In addition, it offers a possible route for seawater desalination (14). However, the scalable production of hydrogen from seawater electrolysis still faces many challenges.

The chlorine evolution reaction (CER), an unintentional reaction that occurs due to the presence of chloride ions in seawater, poses the greatest challenge since it will compete with the desired oxygen evolution reaction (OER) on the anode. Although OER is thermodynamically more favorable, with an onset potential ~480 mV lower than that of CER in alkaline conditions, the OER kinetics are more sluggish because the reaction involves a complex four-electron transfer process, while CER requires the transfer of only two electrons (15–17). Accordingly, the overpotential required for OER in alkaline seawater electrolysis should be significantly lower than 480 mV to avoid triggering the CER process. Another challenge in seawater electrolysis results from the highly corrosive seawater that also contains bacteria and microbes, all of which will corrode and poison catalysts (18). Additionally, some insoluble precipitates, such as $Mg(OH)_2$ and $Ca(OH)_2$, will be generated on the cathode due to local pH change and will cover the catalyst surface and decay the overall seawater-splitting efficiency (12). Therefore, the primary task for advancing seawater electrolysis technology is seeking active and stable anode materials for selective OER over CER. Layered double hydroxides (LDHs) have been demonstrated to be among the most active OER electrocatalysts in alkaline freshwater splitting (19). Recently, a series of LDH-based electrocatalysts, including NiFe LDH (20), NiFe LDH/NiS (21), V-doped CoCr LDH (22), CeO_{2-x}@CoFe LDH (23), and B-modified CoFe LDH (24), have also been utilized for OER in seawater electrolytes, exhibiting fairly good performance with

Author affiliations: [a]Department of Chemistry, The Chinese University of Hong Kong, Hong Kong SAR 999077, China; [b]Department of Physics, University of Houston, Houston, TX 77204; [c]Texas Center for Superconductivity, University of Houston, Houston, TX 77204; [d]College of Physical Science and Technology, Central China Normal University, Wuhan 430079, China; and [e]Institute for Advanced Materials, Hubei Normal University, Huangshi 435002, China

Author contributions: L.Y. designed research; L.Y., J.X., C.H., J.Z., and M.Q. performed research; L.Y. and Y.Y. analyzed data; L.Y., Z.R., C.-W.C., and J.C.Y. wrote the paper; and Z.R., C.-W.C., and J.C.Y. led the project.

Reviewers: J.C., Hunan University; Y.D., Beihang University; G.W., University at Buffalo, State University of New York; and Z.J.X., Nanyang Technological University.

The authors declare no competing interest.

[1]To whom correspondence may be addressed. Email: zren@uh.edu, cwchu@uh.edu, and jimyu@cuhk.edu.hk.

This article contains supporting information online at http://www.pnas.org/lookup/suppl/doi:10.1073/pnas.2202382119/-/DCSupplemental.

Published April 27, 2022.

overpotentials well below 480 mV at large current densities (e.g., 500 mA cm^{-2}) and thus show great potential for seawater electrolysis. On the other hand, recent studies have proved that introducing additional transition metals into LDH materials is an effective strategy for boosting OER activity since the introduced metals not only provide extra metal sites but also work as modulators to regulate the electronic structure of the host LDH catalyst, finally optimizing the adsorption energy of OER intermediates (25). For example, Li et al. reported a V-doped NiFe LDH electrocatalyst for efficient OER in alkaline freshwater media and found that the doped V acts as an electronic modulator to enhance conductivity for rapid electron transfer, as well as induces a strong electronic interaction with neighboring Fe sites to lower the energy barrier of the OER process (26). Reports of similar catalysts, including W-doped NiFe LDH (27), Fe-incorporated CoNi LDH (28), Rh-doped CoFe LDH (29), and Ir-doped NiV LDH (30), showed that the introduced transition metals accelerate the OER kinetics via modifying electronic structures for lower potential barriers, promoting conductivity for high charge-transfer efficiency, and tuning nanostructures for more active sites.

Here, we report a CuCo LDH coincorporated with Ni and Fe (denoted as NiFe-CuCo LDH) that is derived from CuCo metal-organic frameworks (MOFs) and serves as a homogeneous multimetallic OER catalyst for alkaline seawater electrolysis. The dual-metal coincorporated LDH was fabricated through a simultaneous etching-incorporation-sedimentation process, which induces a structural reorganization from the original microsheet arrays of the MOFs into ultrathin hierarchical micronanosheet arrays of the LDHs. This ingenious micronanoscale allows a maximum exposure of abundant active sites and expedites electrolyte diffusion for fast mass transport. Moreover, the introduced Ni and Fe synergistically modulate the electronic structure of CuCo LDH, which not only enhances electrical conductivity for efficient charge transfer but also promotes corrosion resistance against the aggressive corrosive properties of seawater. Consequently, the NiFe-CuCo LDH catalyst exhibits high OER performance toward seawater electrolysis, delivering current densities of 100, 300, and 500 mA cm^{-2} at small overpotentials of 259, 278, and 283 mV, respectively, in a harsh 6 M KOH seawater electrolyte, accompanied by high selectivity (Faradaic efficiency [FE] of 97.4% for O_2 at 500 mA cm^{-2}) and good stability (increased overpotential of ~71 mV after 500 h electrolysis at 500 mA cm^{-2}). Such a high performance establishes our multimetallic electrocatalyst as one of the best OER catalysts for alkaline seawater electrolysis reported thus far, advancing the development of seawater electrolysis.

Results and Discussion

Catalyst Synthesis and Characterization. As schematically illustrated in Fig. 1*A*, the NiFe-CuCo LDH catalyst was converted from well-known Co-based MOFs (CuCo MOFs) (31), which were first synthesized on Ni foam using a previously reported room temperature coprecipitation approach (32). It should be noted that bimetallic CuCo MOFs, rather than Co MOFs, were selected since CuCo MOFs have demonstrated higher OER activity due to electronic band structure modulation resulting from the addition of Cu atoms (33). The scanning electron microscopy (SEM) images in *SI Appendix*, Fig. S1 show that the as-received Ni foam substrate has a three-dimensional (3D) porous structure with a smooth surface. Following the growth of CuCo MOFs, its surface is fully covered by many vertically aligned microsheet arrays (Fig. 1*B*) with uniform dispersion of elemental Co, Cu, C, and N (*SI Appendix*, Fig. S2) and a thickness of about 12 μm (*SI Appendix*, Fig. S3). In the second step, one piece of the as-prepared CuCo MOFs was immersed into an aqueous solution containing $Ni(NO_3)_2$ and $FeSO_4$ for 1 h at room temperature to obtain the final NiFe-CuCo LDH catalyst (Fig. 1*A*). A color change can be clearly seen after each of the two steps; the uniform violet color of the CuCo MOFs film is transformed into the earthy yellow color of the NiFe-CuCo LDH catalyst (*SI Appendix*, Fig. S4). This transformation follows an etching-incorporation-sedimentation mechanism (29, 34). First, due to the hydrolysis of Ni^{2+} and Fe^{2+}, the aqueous solution of $Ni(NO_3)_2$ and $FeSO_4$ provides a weakly acidic environment, in which H^+ ions would etch CuCo MOFs via breaking the coordination bonds between Co/Cu atoms and organic linkers. Similar to Ni^{2+} and Fe^{2+}, the released Co^{2+}/Cu^{2+} also undergo a reversible hydrolysis process to generate $Co(OH)_2/Cu(OH)_2$ and H^+ ions (34). As the etching process consumes more H^+ ions, the hydrolysis of the metal ions accelerates to produce more metal hydroxides, which are finally cosedimented into the resulting LDHs. Meanwhile, Ni and Fe are simultaneously incorporated into the CuCo LDH through an anion exchange process (28). Additionally, a small amount of NiFe LDH is generated due to spontaneous oxidation of Fe^{2+} in the air (20). Therefore, the final NiFe-CuCo LDH catalyst should be composed of Ni/Fe coincorporated CuCo LDH along with some NiFe LDH.

Fig. 1 *C* and *D* display low-magnification SEM images of the NiFe-CuCo LDH catalyst, from which it can be observed that the multimetallic catalyst inherits the microsheet array morphology from the initial MOFs without the etching process causing any collapse, although it does induce some roughness on the microsheet surfaces. The high-magnification SEM image in Fig. 1*E* clearly shows that many nanosheets uniformly stand on the entire surface of each microsheet, rendering a favorable hierarchical micronanosheet structure that effectively suppresses the aggregation of LDH nanosheets and creates a large surface area. The thickness of a single hybrid micronanosheet array is around 300 nm (*SI Appendix*, Fig. S5 *A* and *B*). The transmission electron microscopy (TEM) image in Fig. 1*F* further confirms this hierarchical micronanosheet architecture and shows that all nanosheets are perpendicularly anchored on the microsheet surfaces, giving rise to adequate interspaces for electrolyte permeation and gas bubble release. These vertically aligned nanosheets exhibit a densely wrinkled feature (Fig. 1*G*) and are only ~4.9 nm thick (*SI Appendix*, Fig. S5 *C* and *D*), which is expected to enable more edge active sites for catalytic reactions (35). The high-resolution TEM (HRTEM) image in Fig. 1*H* shows distinguishable lattice fringes with interplanar spacings of 0.24 and 0.26 nm, which are assigned to the (015) plane of NiFe LDH and the (102) plane of CuCo LDH, respectively. The selective area electron diffraction (SAED) pattern in Fig. 1*I* displays well-resolved diffraction rings belonging to the (102) and (113) planes of CuCo LDH (Powder Diffraction File [PDF] #46-606) and the (015) plane of NiFe LDH (PDF#42-573). Fig. 1*J* shows the high-angle annular dark-field scanning TEM (HAADF-STEM) image and corresponding elemental mapping images of NiFe-CuCo LDH, which clearly verify the existence and homogenous distribution of Ni, Fe, Co, Cu, and O in the hierarchical micronanosheet arrays. To study the effect of coincorporation, two control samples, Ni-incorporated CuCo LDH and Fe-incorporated CuCo LDH (designated Ni-CuCo LDH and Fe-CuCo LDH, respectively), were also successfully synthesized by the same method for

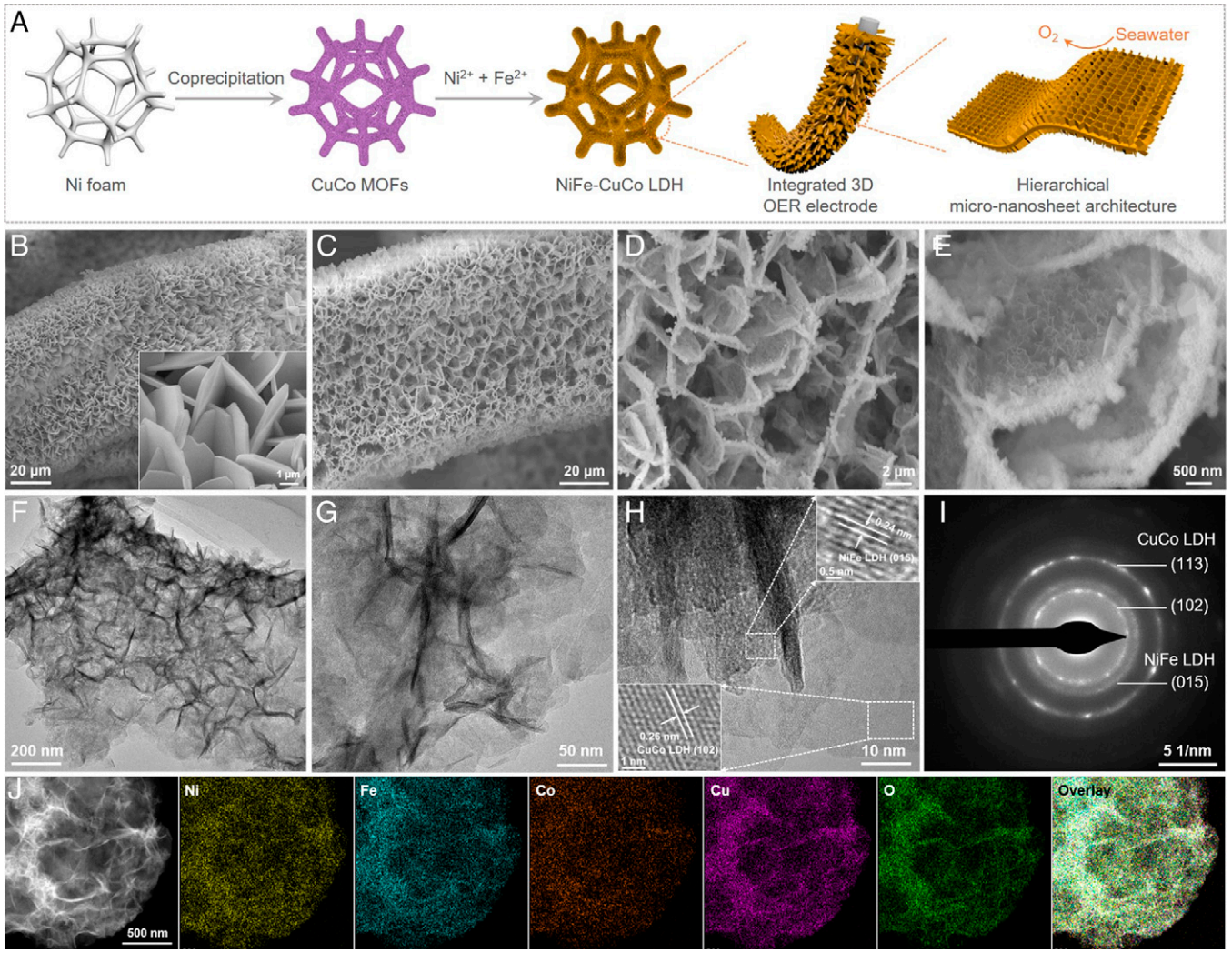

Fig. 1. Catalyst synthesis and characterization. (*A*) Schematic illustration of the synthesis process for the hierarchical NiFe-CuCo LDH micronanosheet catalyst. SEM images of CuCo MOFs (*B*) and NiFe-CuCo LDH at different magnifications (*C*–*E*). TEM images (*F, G*), HRTEM image (*H*), SAED pattern (*I*), and HAADF-STEM image and corresponding elemental mapping of NiFe-CuCo LDH (*J*).

comparison (*SI Appendix*, Fig. S4). *SI Appendix*, Figs. S6 and S7 present their respective SEM and energy-dispersive X-ray spectroscopy (EDS) mapping images, which show that the control samples also exhibit hierarchical morphology, although it is slightly different from that of NiFe-CuCo LDH.

To determine the exact physical phase of each catalyst, we first conducted X-ray diffraction (XRD) for the different samples. As shown in Fig. 2*A*, besides three strong diffraction peaks from the Ni substrate, the XRD pattern of the CuCo MOF sample exhibits typical diffraction peaks (5° to 45°) corresponding to zeolitic imidazolate frameworks (ZIF-67) (36). Upon the solution treatment, all of these peaks from ZIF-67 disappear, suggesting a complete phase transformation. At the same time, a broad peak located at ∼22.6° shows up, which is indexed to the (006) plane of LDH materials (28, 37), demonstrating the successful conversion of MOFs into LDHs. Raman spectra in Fig. 2*B* further affirm this conversion since the peaks from the CuCo MOF spectrum are absent from those of the three LDH samples. Instead, three peaks at ∼452, 530, and 1,046 cm^{-1}, ascribed to the representative stretching modes of LDHs, are detected (20). Notably, the peak at 530 cm^{-1} shows a positive shift in the NiFe-CuCo LDH catalyst, which may be induced by the strong electronic interactions between the multiple metals resulting from Ni/Fe coincorporation. We then performed X-ray photoelectron spectroscopy (XPS) measurements to investigate the chemical states and electronic structures of the three LDH catalysts. As the high-resolution XPS spectra of Co 2p in Fig. 2*C* show, that of the Ni-CuCo LDH catalyst exhibits two spin-orbit peaks at 780.9 eV for Co $2p_{3/2}$ and 797.0 eV for Co $2p_{1/2}$, accompanied by two satellite peaks (each denoted as "Sat."), indicating the coexistence of Co^{3+} and Co^{2+} (38). For the Fe-CuCo LDH and NiFe-CuCo LDH spectra, the two spin-orbit peaks show a negative shift to lower binding energy, suggesting an electronic structure change of Co caused by Fe incorporation. In Fig. 2*D*, the Cu 2p XPS spectra exhibit two peaks at 934.1 and 952.3 eV for Cu $2p_{3/2}$ and Cu $2p_{1/2}$, respectively, as well as a visible satellite peak at ∼942.1 eV, suggesting that Cu is in a Cu^{2+} oxidation state in the three LDH catalysts (39). The high-resolution Ni 2p spectrum of Ni-CuCo LDH features Ni $2p_{3/2}$ and Ni $2p_{1/2}$ peaks at 855.1 and 872.9 eV, respectively, together with two satellite peaks (Fig. 2*E*), which is indicative of the Ni^{2+} oxidation state (30). Similar to the Co 2p spectra, a negative shift is also observed in the Ni $2p_{3/2}$ and Ni $2p_{1/2}$ peaks of the NiFe-CuCo LDH spectrum. In the Fe 2p XPS spectrum of Fe-CuCo LDH (Fig. 2*F*), the two typical peaks located at 710.8 and 724.1 eV are ascribed to Fe $2p_{3/2}$ and Fe $2p_{1/2}$, respectively, and two satellite peaks are detected at 717.1 and 731.9 eV, suggesting that

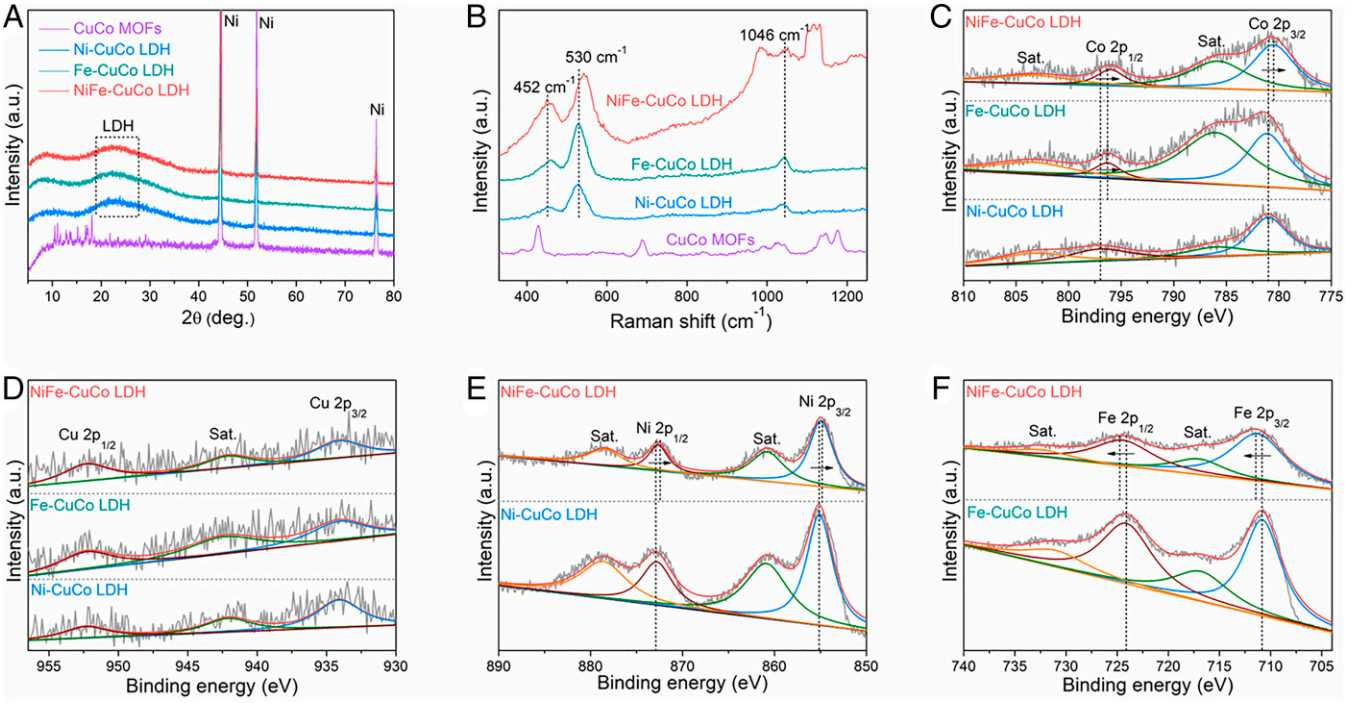

Fig. 2. XRD patterns (*A*) and Raman spectra (*B*) of different catalysts. High-resolution XPS of Co 2p (*C*), Cu 2p (*D*), Ni 2p (*E*), and Fe 2p (*F*) for Ni-CuCo LDH, Fe-CuCo LDH, and NiFe-CuCo LDH.

Fe^{3+} is the dominant chemical state on the surface (40). In the corresponding spectrum for the NiFe-CuCo LDH catalyst, the two spin-orbit peaks of Fe $2p_{3/2}$ and Fe $2p_{1/2}$ clearly show a positive shift to higher binding energy resulting from the strong interactions between the different metals. Taken together, these results attest to the successful transformation from MOFs to LDHs with modified electronic configurations due to Ni and Fe coincorporation, which may favor the adsorption of OER intermediates and thus boost the OER activity (41).

OER Performance in Alkaline Freshwater Electrolyte. According to the Pourbaix diagram, the difference between the onset potential values of OER and CER reaches a maximum of ∼480 mV when the electrolyte pH is larger than 7.5 (17), indicating that an alkaline environment is more favorable for selective OER over CER during seawater electrolysis. Therefore, to clearly compare OER activity, we first assessed the different catalysts, including the benchmark RuO_2 and IrO_2 catalysts loaded on Ni foam, in 1 M KOH freshwater electrolyte. As the polarization curves in Fig. 3*A* show, all three LDH catalysts exhibit significantly enhanced OER activity relative to the original CuCo MOFs, especially Ni-CuCo LDH and NiFe-CuCo LDH, which are also superior to the benchmark RuO_2 and IrO_2 (*SI Appendix*, Fig. S8) catalysts. Moreover, with Ni and Fe coincorporation, the multimetallic NiFe-CuCo LDH catalyst exhibits the highest OER activity among the five catalysts. It requires an overpotential of only 212 mV to reach the benchmark current density of 10 mA cm^{-2}, which is much smaller than the corresponding values for the Ni-CuCo LDH, Fe-CuCo LDH, and RuO_2 catalysts, as shown by the comparison in Fig. 3*B*. Meanwhile, at a potential of 1.5 V vs. reversible hydrogen electrode (RHE), our NiFe-CuCo LDH catalyst delivers a current density up to 141 mA cm^{-2}, which is nearly 2.8 and 16.8 times that of Ni-CuCo LDH and Fe-CuCo LDH, respectively, and represents a 63-fold improvement compared with commercial RuO_2 (Fig. 3*B*), as well as being significantly higher than that of the well-recognized NiFe LDH catalyst (*SI Appendix*, Fig. S9), demonstrating superior OER activity. It should be noted that the reduction peaks between 1.3 and 1.4 V vs. RHE in the polarization curves of Ni-CuCo LDH and NiFe-CuCo LDH result from the reduction of Ni^{3+} to Ni^{2+} (42). *SI Appendix*, Fig. S10 further shows the performance of NiFe-CuCo LDH at large current densities. To achieve current densities of 100, 500, and 1,000 mA cm^{-2}, it requires overpotentials of 262, 300, and 345 mV, respectively, all of which are far lower than 480 mV. We also investigated the effects of $Ni(NO_3)_3/FeSO_4$ concentration and reaction time in the second synthesis step on the OER activity of the final NiFe-CuCo LDH catalysts. The sample prepared with 0.15 M $Ni(NO_3)_3/FeSO_4$ and a reaction time of 1 h was found to exhibit the best OER activity (*SI Appendix*, Figs. S11 and S12) and was used for further analyses unless otherwise stated. In Fig. 3*C*, a small Tafel slope of 48.3 mV dec^{-1} was measured for the NiFe-CuCo LDH catalyst in comparison with that of the Ni-CuCo LDH (64.4 mV dec^{-1}), Fe-CuCo LDH (64.9 mV dec^{-1}), RuO_2 (93.6 mV dec^{-1}), and CuCo MOF (100.5 mV dec^{-1}) electrodes, suggesting favorable and fast OER kinetics. Given the very small values of its overpotential at 10 mA cm^{-2} and its Tafel slope, our NiFe-CuCo LDH catalyst outperforms most recently reported transition-metal-based electrocatalysts (Fig. 3*D*), including some multimetallic electrocatalysts such as NiFeMn LDH (43), NiCoFe MOFs (44), and V-doped CoNiB (45), establishing it as among the first-class nonprecious OER electrocatalysts.

To understand the origins of the high activity of NiFe-CuCo LDH, we first calculated the electrochemically active surface area (ECSA) of each as-prepared catalyst through the determination of its double-layer capacitance (C_{dl}) from cyclic voltammetry curves (*SI Appendix*, Fig. S13) (46). As expected, the NiFe-CuCo LDH catalyst exhibits the largest ECSA among the four catalysts measured (*SI Appendix*, Fig. S14*A*), offering more

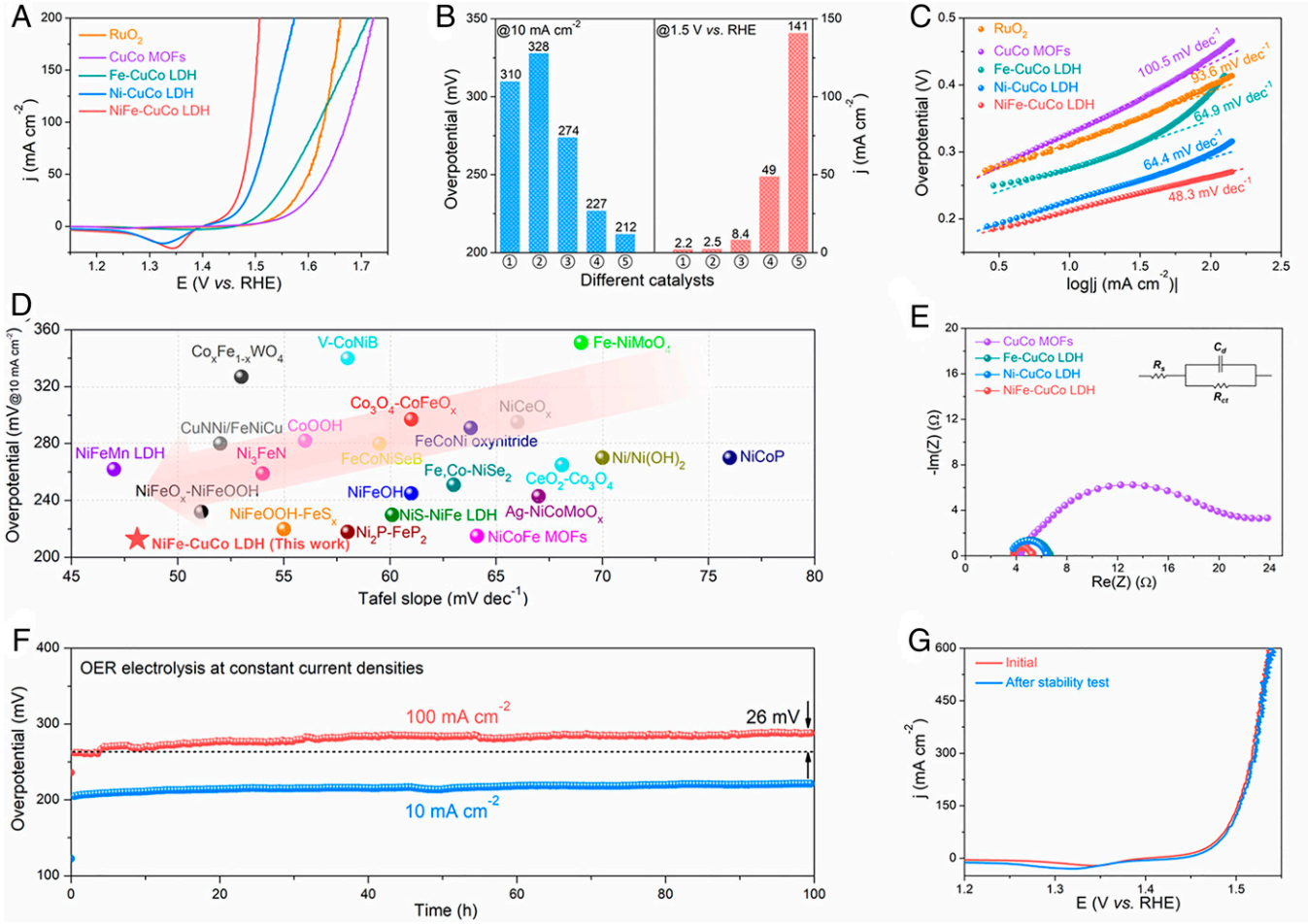

Fig. 3. OER performance in 1 M KOH. OER polarization curves (*A*), comparisons of the overpotential required at 10 mA cm^{-2} and the current density achieved at 1.5 V vs. RHE (the numbers in the circles denote the catalysts in order from RuO_2 to NiFe-CuCo LDH as shown in the legend for *A*) (*B*), and Tafel plots derived from *A* for different catalysts (*C*). (*D*) Comparison of Tafel slope values and overpotentials required at 10 mA cm^{-2} between the NiFe-CuCo LDH catalyst and other recently reported transition-metal-based OER electrocatalysts. (*E*) EIS Nyquist plots of different catalysts. *Inset*: the equivalent circuit. (*F*) Long-term stability tests of NiFe-CuCo LDH at constant current densities of 10 and 100 mA cm^{-2}. (*G*) Polarization curves of NiFe-CuCo LDH before and after the stability test at 100 mA cm^{-2}.

active sites for OER. Nevertheless, after normalizing the polarization curves by ECSA, the NiFe-CuCo LDH catalyst still exhibits higher OER activity than the other three (*SI Appendix*, Fig. S14*B*), suggesting that its excellent performance cannot be merely attributed to the improved ECSA from the unique micronanosheet morphology, but to higher intrinsic catalytic activity benefiting from Ni and Fe coincorporation. In this regard, electrochemical impedance spectroscopy (EIS) was utilized to comprehend the effect of Ni/Fe coincorporation on OER kinetics. As the EIS Nyquist plots in Fig. 3*E* show, the NiFe-CuCo LDH catalyst has a much smaller charge-transfer resistance (R_{ct}) of 1.45 Ω than Ni-CuCo LDH (2.66 Ω), Fe-CuCo LDH (2.79 Ω), and CuCo MOFs (18.3 Ω), indicating a more efficient charge transfer at the electrode/electrolyte interface that is contributed by the coincorporation of Ni and Fe (47). Remarkably, in addition to its high OER activity, the NiFe-CuCo LDH electrode exhibits very good OER stability in 1 M KOH. As displayed in Fig. 3*F*, the overpotentials at fixed current densities of 10 and 100 mA cm^{-2} show increases of 12 and 26 mV, respectively, during 100 h OER catalysis at each current density, which are negligible relative to that of the benchmark IrO_2 catalyst (*SI Appendix*, Fig. S15), and the polarization curve obtained after the stability test at 100 mA cm^{-2} remains nearly unchanged from that prior to the test (Fig. 3*G*), demonstrating superior OER stability in alkaline freshwater electrolyte.

OER Performance in Alkaline Seawater Electrolytes. After confirming its improved OER activity in alkaline freshwater electrolyte, we then evaluated the seawater OER performance of the NiFe-CuCo LDH electrode in alkaline simulated-seawater (1 M KOH + 0.5 M NaCl and 1 M KOH + 1.5 M NaCl) and alkaline natural-seawater (1 M KOH + seawater) electrolytes. As shown in Fig. 4 *A* and *B*, compared with its activity in 1 M KOH, the NiFe-CuCo LDH catalyst continues to exhibit excellent OER activity with little decay in alkaline simulated-seawater electrolytes, signifying that the highly concentrated Cl ions have little impact on the catalytic activity and, in turn, that the catalyst achieves high OER selectivity. In alkaline natural-seawater electrolyte (1 M KOH + seawater), retrogression of the electrode's activity is clearly observed and mostly results from the bacteria and microbes in the seawater, as well as from some insoluble precipitates in the electrolyte generated during seawater OER catalysis (48). Very impressively, as shown in Fig. 4*B*, our NiFe-CuCo LDH electrode still outputs large current densities of 100 and 500 mA cm^{-2} at low overpotentials of 315 and 355 mV, respectively, which are well below the 480-mV overpotential required to trigger CER. To explore the possibility of practical application, we further tested the electrode's OER performance in a very harsh seawater electrolyte of 6 M KOH + seawater. As shown in Fig. 4*C*, the OER activity is further promoted, affording current

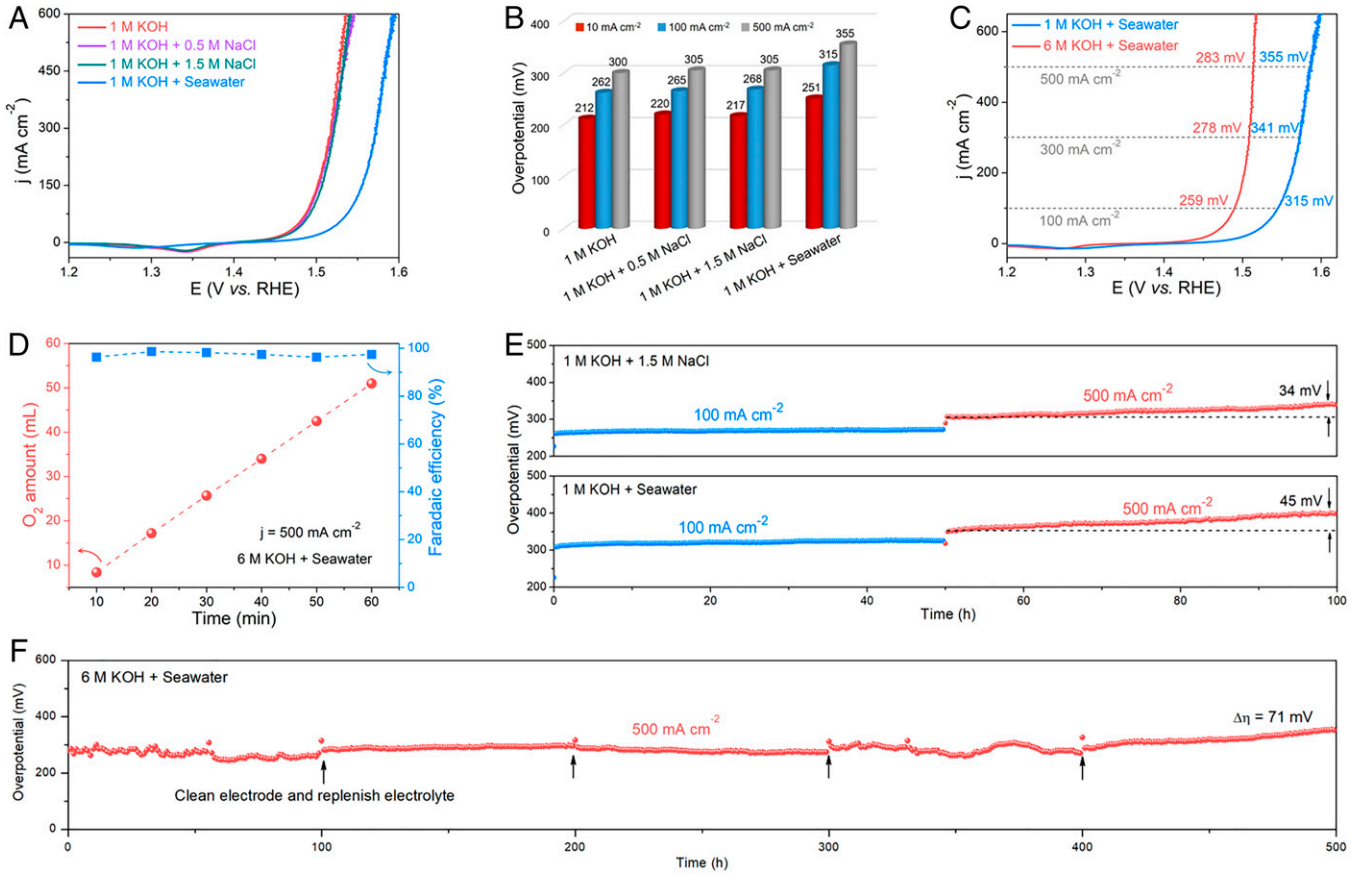

Fig. 4. OER performance in alkaline seawater electrolytes. Polarization curves (*A*) and comparison of the overpotentials required to achieve current densities of 10, 100, and 500 mA cm^{-2} for the NiFe-CuCo LDH catalyst in different electrolytes (*B*). (*C*) Polarization curves of NiFe-CuCo LDH in 1 M KOH + seawater and 6 M KOH + seawater electrolytes. (*D*) Blue squares: FE of NiFe-CuCo LDH measured at 500 mA cm^{-2} in 6 M KOH + seawater electrolyte. Red circles: O_2 generated during the FE test. (*E*) Long-term stability tests at constant current densities of 100 and 500 mA cm^{-2} for the NiFe-CuCo LDH catalyst in 1 M KOH + 1.5 NaCl and 1 M KOH + seawater electrolytes. (*F*) Long-term stability test at a constant current density of 500 mA cm^{-2} for the NiFe-CuCo LDH catalyst in 6 M OH + seawater electrolyte for up to 500 h. The electrode was cleaned and the electrolyte was replenished every 100 h as indicated by the arrows.

densities of 100 and 300 mA cm^{-2} at extremely low overpotentials of 259 and 278 mV, respectively, and even a record-low overpotential of 283 mV to achieve the industrially required current density of 500 mA cm^{-2}. The polarization curve for OER in 6 M KOH + seawater was also recorded without iR compensation for comparison (*SI Appendix*, Fig. S16), and the performance is clearly worse than that with iR compensation (49). In addition, the NiFe-CuCo LDH electrode shows a very high average FE of 97.4% for OER at a large current density of 500 mA cm^{-2} in the harsh seawater electrolyte (Fig. 4*D*), suggesting that the total electron transfer during seawater electrolysis is dominated by the desired OER, not CER.

The issue of stability is another obstacle that impedes the practical application of seawater electrolysis. Therefore, we examined the operating durability of NiFe-CuCo LDH by conducting long-term OER electrolysis under constant current densities in three different alkaline seawater electrolytes. Fig. 4*E* shows that, in both 1 M KOH + 1.5 M NaCl and 1 M KOH + seawater electrolytes, NiFe-CuCo LDH functions quite stably with ignorable degradation over 50 h of electrolysis at a constant current density of 100 mA cm^{-2}. Under a larger current density of 500 mA cm^{-2}, some attenuation is observed, but the increase in overpotential still does not exceed 45 mV. Impressively, our NiFe-CuCo LDH electrode also displays excellent durability in the harsh seawater electrolyte (6 M KOH + seawater). As shown in *SI Appendix*, Fig. S17, the overpotential is found to increase by only ∼18 mV over 100 h of operation at a constant current density of 100 mA cm^{-2}. In sharp contrast, the overpotential of IrO_2 under the same condition increases by more than 100 mV over 100 h of operation (*SI Appendix*, Fig. S18). For our NiFe-CuCo LDH electrode, even under a large current density of 500 mA cm^{-2}, the overpotential only slightly increases by ∼71 mV after up to 500 h of electrolysis for a degradation rate of 0.142 mV h^{-1} (Fig. 4*F*), confirming the superior durability of this anode material that is promising for practical application. After 500 h of seawater electrocatalysis in the harsh condition, we further found that the hierarchical micronanosheet morphology of the NiFe-CuCo LDH catalyst is well preserved except for a few nanosheets peeling off from the microsheets, as proved by SEM, TEM, and atomic force microscopy (AFM) results (*SI Appendix*, Figs. S19–S21, respectively), indicating robust structural stability with a high capacity to resist the driving force from the gas bubbles during large-current-density electrolysis. Additionally, XRD patterns and high-resolution XPS spectra further reveal that the LDH phase and chemical composition of the NiFe-CuCo LDH surface remain unchanged after testing (*SI Appendix*, Figs. S22 and S23, respectively), demonstrating the catalyst's good chemical stability in seawater.

Mechanism Study. To elucidate such remarkable stability, we carried out corrosion testing on different as-prepared catalysts in natural seawater, and *SI Appendix*, Fig. S24 displays the corresponding corrosion polarization curves. From the results in Fig. 5*A*, it can be seen that after converting MOFs into LDHs,

the corrosion potential (E_{corr}) is increased while the corrosion current density (j_{corr}) is decreased, suggesting enhanced corrosion resistance. More importantly, with Ni and Fe coincorporation, NiFe-CuCo LDH exhibits the highest E_{corr} and the lowest j_{corr} among the three LDH catalysts, proving its highest corrosion resistance in seawater, which contributes to the outstanding stability. To unveil the mechanism of how Ni and Fe enhance the anticorrosion property of CuCo LDH, theoretical calculations based on density functional theory (DFT) were performed to study the CER process using a two-step Volmer–Heyrovsky mechanism, which proceeds through the adsorption of Cl^- and subsequent release of molecular Cl_2 (50). The crystal structures of CuCo LDH incorporating Ni atoms, Fe atoms, and both Ni and Fe atoms were adopted as calculation models for Ni-CuCo LDH, Fe-CuCo LDH, and NiFe-CuCo LDH, respectively (*SI Appendix*, Fig. S25). To examine the effect of Ni/Fe incorporation, we focused on Cl^- adsorption on Co and Cu sites (Fig. 5*B*). As the free energy diagrams in Fig. 5 *C* and *D* show, both Co and Cu sites of NiFe-CuCo LDH exhibit much higher adsorption free energy toward Cl^- compared with that for Ni-CuCo LDH and Fe-CuCo LDH, which suggests that Cl^- adsorption on the NiFe-CuCo LDH surface is more difficult than on either the Ni-CuCo LDH or Fe-CuCo LDH surface, thus protecting the catalyst against the corrosive Cl^- and enhancing the anticorrosion property. Due to the sluggish Cl^- adsorption, the CER process is significantly inhibited on NiFe-CuCo LDH relative to the other two catalysts. Specifically, the theoretical overpotentials for CER were calculated to be 3.70 and 1.93 V for Co and Cu sites, respectively, of NiFe-CuCo LDH, which are notably higher than the overpotentials for OER observed in the polarization curves. This also explains why OER is more favorable than the competitive CER on the NiFe-CuCo LDH catalyst and thus why the catalyst achieves high OER selectivity.

SI Appendix, Table S1 presents a detailed comparison between the NiFe-CuCo LDH catalyst and other recently reported OER electrocatalysts in alkaline seawater electrolytes. In terms of activity, selectivity, and stability, our NiFe-CuCo LDH electrode is one of the most efficient OER electrocatalysts for alkaline seawater electrolysis reported to date. Its high seawater oxidation performance is mainly ascribed to the following factors. First, the 3D hierarchical micronanosheet arrays not only provide an extremely large surface area for abundant active sites but also avail electrolyte diffusion and gas product release for rapid mass transport. Second, the incorporated Ni and Fe effectively promote the electrical conductivity, which accelerates charge transfer between the catalyst surface and the electrolyte, thus boosting the OER kinetics. Third, the strong interactions between different metal sites in the multimetallic catalyst regulate its electronic structure, improving the intrinsic activity of

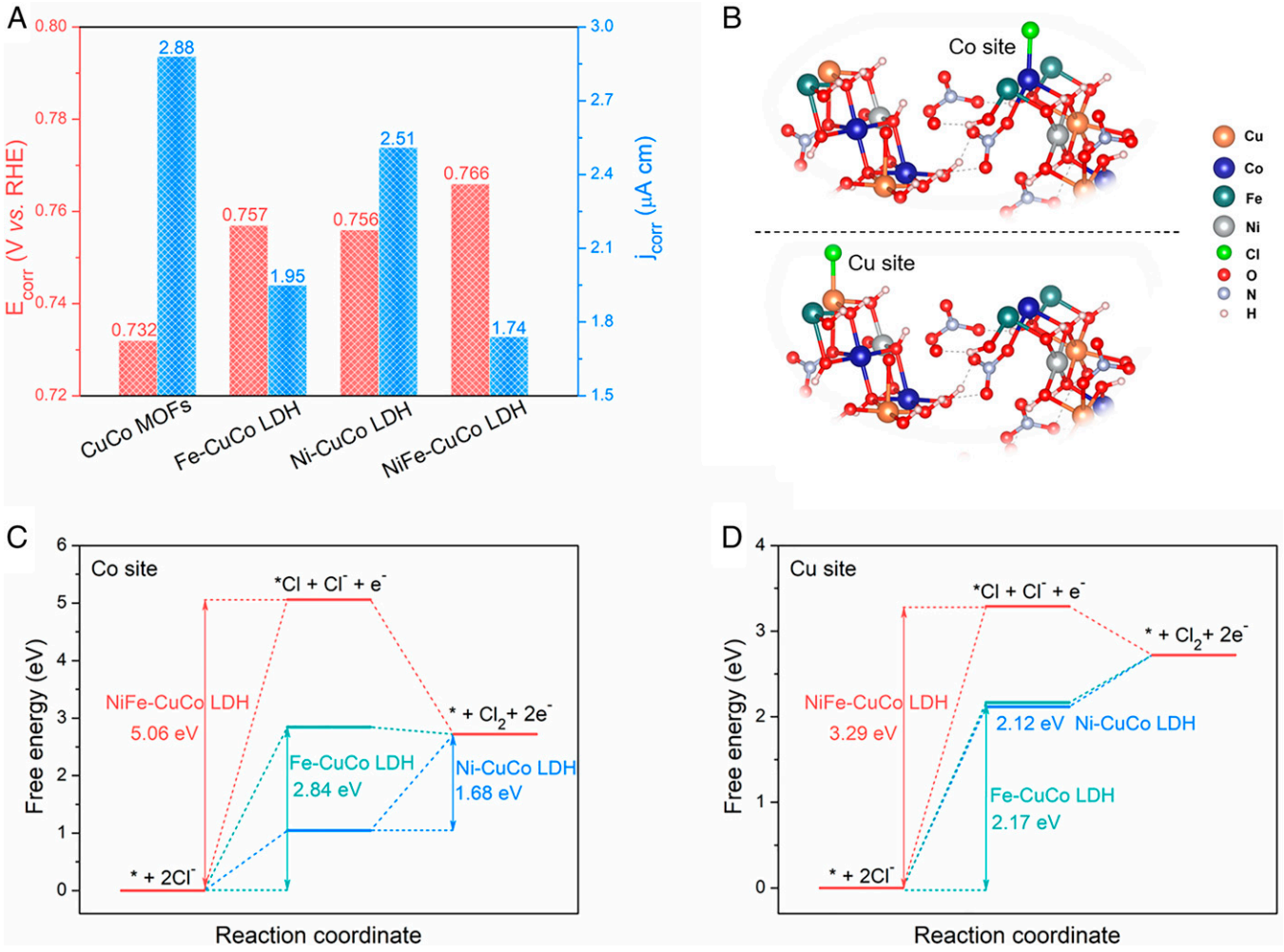

Fig. 5. (*A*) E_{corr} and j_{corr} of different catalysts in natural seawater. (*B*) Cl^- adsorption on Co and Cu sites of the optimized atomic structure of NiFe-CuCo LDH. Free energy diagrams of CER on Co (*C*) and Cu (*D*) sites of Fe-CuCo LDH, Ni-CuCo LDH, and NiFe-CuCo LDH, where * represents an active site on the catalyst surface.

the catalytic centers (41). Finally, the coincorporated Ni and Fe synergistically enhance the corrosion resistance of CuCo LDH through inactivation of Cl^- adsorption to resist the aggressive seawater, which endows the catalyst with good durability.

Conclusions

In summary, we have developed an active, stable, and low-cost OER electrode composed of Ni/Fe coincorporated CuCo LDH ultrathin micronanosheet arrays derived from MOFs through a facile solution treatment. Benefiting from the high density of exposed active sites and improved mass transport rendered by the hierarchical structure, along with the accelerated charge transfer and enhanced corrosion resistance contributed by the introduced Ni and Fe, the obtained electrode shows excellent seawater oxidation performance with extremely low overpotentials of 278 and 283 mV required to achieve large current densities of 300 and 500 mA cm^{-2}, respectively, in 6 M KOH seawater electrolyte. It also exhibits high OER selectivity, and its good durability is shown by its survival during operation at a constant current density of 500 mA cm^{-2} with only very slightly increased overpotential after 500 h. This work presents an efficient OER electrode produced from well-recognized materials, which we believe represents a giant step in advancing seawater electrolysis technology.

Materials and Methods

Chemicals. Fe (II) sulfate heptahydrate ($FeSO_4{\cdot}7H_2O$, analytical reagent; Riedel-de Haen), Ni (II) nitrate hexahydrate [$Ni(NO_3)_2{\cdot}6H_2O$, 98%, analytical reagent], Co (II) nitrate hexahydrate [$Co(NO_3)_2{\cdot}6H_2O$, 99%; Aladdin], Cu (II) nitrate trihydrate [$Cu(NO_3)_2{\cdot}3H_2O$, analytical purity; Sinopharm Chemical Reagent Co., Ltd.], 2-methylimidazole ($C_4H_6N_2$, 98%; Aladdin), ruthenium dioxide (RuO_2; Alfa Aesar), iridium dioxide (IrO_2; Alfa Aesar), Nafion (117 solution, 5% wt; Aldrich), hydrochloric acid (HCl, 37%; RCI Labscan Limited), potassium hydroxide (KOH, 99.99%; Aladdin), and Ni foam (thickness, 1.6 mm) were used as received. Deionized (DI) water was used for the preparation of all aqueous solutions. Natural seawater (pH ~8.2) was collected from Tolo Harbor near the Chinese University of Hong Kong, New Territories, Hong Kong SAR, China.

Synthesis of NiFe-CuCo LDH. The NiFe-CuCo LDH catalyst was synthesized on Ni foam using a two-step approach, the first of which is the synthesis of CuCo MOFs via a previously reported coprecipitation approach (32). Prior to the synthesis, we cleaned the Ni foam substrate by putting one piece of commercial Ni foam (2 cm × 5 cm) into 3 M HCl, ethanol, and DI water in sequence for ultrasonic treatment for several minutes. We then prepared two aqueous solutions, one of which contains 40 mL of 0.04 M $Co(NO_3)_2{\cdot}6H_2O$ and 0.01 M $Cu(NO_3)_2{\cdot}3H_2O$ and another of which contains 40 mL 0.4 M $C_4H_6N_2$. The two solutions were quickly mixed together, and the cleaned Ni foam substrate was immediately immersed into the mixture solution. After 4 h of reaction at room temperature, the sample was removed from the mixture solution, rinsed with DI water, and dried at 60 °C overnight. In the second step, one piece of the as-prepared CuCo MOFs grown on Ni foam (~1 cm × 2 cm) was immersed into a solution containing 10 mL of 0.15 M $Ni(NO_3)_2{\cdot}6H_2O$ and 0.15 M $FeSO_4{\cdot}7H_2O$ for 1 h at room temperature. The sample was finally removed from the solution, washed with DI water, and dried in air before use. For comparison, two control samples of Ni-CuCo LDH and Fe-CuCo LDH were also synthesized in the same way except that the solution in the second step was replaced by 0.15 M $Ni(NO_3)_2{\cdot}6H_2O$ only and 0.15 M $FeSO_4{\cdot}7H_2O$ only, respectively. Pure NiFe LDH was also synthesized on Ni foam for comparison using the same method as described in the second step above. In addition, to study the effect of Ni/Fe concentration and reaction time on their catalytic activity, we synthesized a series of different NiFe-CuCo LDH catalysts by changing the concentration of $Ni(NO_3)_2{\cdot}6H_2O/FeSO_4{\cdot}7H_2O$ and the reaction time in the second step. Specifically, 0.05, 0.10, or 0.20 M of $Ni(NO_3)_2{\cdot}6H_2O/FeSO_4{\cdot}7H_2O$ was used in the solution, along with 0.5, 1.5, or 2.0 h of reaction time.

Preparation of RuO_2 and IrO_2 Catalysts on Ni Foam. To prepare the RuO_2 and IrO_2 electrodes for comparison, 40 mg RuO_2 or IrO_2 and 60 μL Nafion were dispersed in 540 μL ethanol and 400 μL DI water in a small sealed tube. The mixture was ultrasonicated for 30 min, and the dispersion was then coated onto a Ni foam substrate, which was dried in air overnight.

Materials Characterization. The morphology and nanostructure of the catalysts were examined by SEM (JEOL JSM-6900) and TEM (FEI TF20) coupled with EDS. AFM characterization was performed using a Bruker AFM system. The phase composition was characterized by XRD (Rigaku SmartLab X-ray diffractometer) with a Cu Kα radiation source. XPS (PHI-Vesoprobe 5000III) was conducted using a Thermo ESCALAB 250Xi spectrometer equipped with an anode of Al Kα radiation (1,486.6 eV) X-ray sources. Raman measurements were performed on a HORIBA LabRAM HR Evolution Raman system with an excitation wavelength of 532 nm.

Electrochemical Tests. All electrochemical tests were performed on an electrochemical station (CHI 760D, CH Instruments, Inc.) in a standard three-electrode cell at room temperature, with an as-prepared sample, a graphite rod, and a standard Hg/HgO electrode serving as the working, counter, and reference electrodes, respectively. Five different electrolytes, including 1 M KOH, 1 M KOH + 0.5 M NaCl, 1 M KOH + 1.5 M NaCl, 1 M KOH + seawater, and 6 M KOH + seawater, were used, and their pH values were 13.79, 13.76, 13.71, 13.65, and 14.60, respectively. The OER polarization curves were obtained at a scan rate of 5 mV s^{-1}, and stability tests were performed under different constant current densities. To calculate FE, we measured the generated gaseous product on the anode by a drainage method in a gas-tight H-cell at a fixed current density of 500 mA cm^{-2} in 6 M KOH + seawater electrolyte. The FE was calculated by comparing the experimentally measured O_2 amount to the theoretically calculated one. EIS was conducted at an overpotential of 300 mV from 0.01 Hz to 100 KHz with an amplitude of 10 mV. All of the measured potentials vs. Hg/HgO were converted to the RHE by the Nernst equation ($E_{RHE} = E_{Hg/HgO} + 0.0591 \times pH + 0.098$). All data have been reported with 85% iR compensation applied manually unless otherwise specified.

DFT Calculations. Theoretical calculations were carried out by using the Vienna Ab-initio Simulation Package (VASP) in Material Studio based on DFT. The generalized gradient approximation (GGA) of Perdew–Burke–Ernzerhof (PBE) form was used to describe the exchange-correction potential. The optimized (012) surface of CuCo LDH incorporating Ni atoms, Fe atoms, and both Ni and Fe atoms were adopted as calculation models for Ni-CuCo LDH, Fe-CuCo LDH, and NiFe-CuCo LDH, respectively.

Data Availability. All study data are included in the article and/or *SI Appendix*.

ACKNOWLEDGMENTS. This work was financially supported by the Research Grants Council General Research Fund of the Hong Kong Special Administrative Region (No. 14304019, 14307620). Z.R. acknowledges support from the Alexander von Humboldt Foundation and Professor Kornelius Nielsch at Leibniz-Institut für Festkörper-und Werkstoffforschung (IFW) Dresden, Germany. C.-W.C. acknowledges support from US Air Force Office of Scientific Research Grants FA9550-15-1-0236 and FA9550-20-1-0068, the T.L.L. Temple Foundation, the John J. and Rebecca Moores Endowment, and the State of Texas through the Texas Center for Superconductivity at the University of Houston.

1. J. A. Turner, Sustainable hydrogen production. *Science* **305**, 972–974 (2004).
2. J. Wang *et al.*, Non-precious-metal catalysts for alkaline water electrolysis: Operando characterizations, theoretical calculations, and recent advances. *Chem. Soc. Rev.* **49**, 9154–9196 (2020).
3. Y. Shi, M. Li, Y. Yu, B. Zhang, Recent advances in nanostructured transition metal phosphides: Synthesis and energy-related applications. *Energy Environ. Sci.* **13**, 4564–4582 (2020).
4. F. Yu *et al.*, Recent developments in earth-abundant and non-noble electrocatalysts for water electrolysis. *Mater. Today Phys.* **7**, 121–138 (2018).
5. Q. Wang *et al.*, Coordination engineering of iridium nanocluster bifunctional electrocatalyst for highly efficient and pH-universal overall water splitting. *Nat. Commun.* **11**, 4246 (2020).
6. H. Zhou *et al.*, Highly active catalyst derived from a 3D foam of $Fe(PO_3)_2/Ni_2P$ for extremely efficient water oxidation. *Proc. Natl. Acad. Sci. U.S.A.* **114**, 5607–5611 (2017).

7. L. A. King *et al.*, A non-precious metal hydrogen catalyst in a commercial polymer electrolyte membrane electrolyser. *Nat. Nanotechnol.* **14**, 1071–1074 (2019).
8. D. Li *et al.*, Highly quaternized polystyrene ionomers for high performance anion exchange membrane water electrolysers. *Nat. Energy* **5**, 378–385 (2020).
9. S. Song *et al.*, Outstanding oxygen evolution reaction performance of nickel iron selenide/stainless steel mat for water electrolysis. *Mater. Today Phys.* **13**, 100216 (2020).
10. S. Fukuzumi, Y. M. Lee, W. Nam, Fuel production from seawater and fuel cells using seawater. *ChemSusChem* **10**, 4264–4276 (2017).
11. S. R. Dresp, F. Dionigi, M. Klingenhof, P. Strasser, Direct electrolytic splitting of seawater: Opportunities and challenges. *ACS Energy Lett.* **4**, 933–942 (2019).
12. W. Tong *et al.*, Electrolysis of low-grade and saline surface water. *Nat. Energy* **5**, 367–377 (2020).
13. L. Yu *et al.*, Non-noble metal-nitride based electrocatalysts for high-performance alkaline seawater electrolysis. *Nat. Commun.* **10**, 5106 (2019).
14. F. Zhang, L. Yu, L. Wu, D. Luo, Z. Ren, Rational design of oxygen evolution reaction catalysts for seawater electrolysis. *Trends Chem.* **3**, 485–498 (2021).
15. Y. Kuang *et al.*, Solar-driven, highly sustained splitting of seawater into hydrogen and oxygen fuels. *Proc. Natl. Acad. Sci. U.S.A.* **116**, 6624–6629 (2019).
16. W. Zang *et al.*, Efficient hydrogen evolution of oxidized Ni-N_3 defective sites for alkaline freshwater and seawater electrolysis. *Adv. Mater.* **33**, e2003846 (2021).
17. F. Dionigi, T. Reier, Z. Pawolek, M. Gliech, P. Strasser, Design criteria, operating conditions, and nickel-iron hydroxide catalyst materials for selective seawater electrolysis. *ChemSusChem* **9**, 962–972 (2016).
18. L. Yu *et al.*, Hydrogen generation from seawater electrolysis over a sandwich-like NiCoN|Ni_xP|NiCoN microsheet array catalyst. *ACS Energy Lett.* **5**, 2681–2689 (2020).
19. L. Wu *et al.*, Recent advances in self-supported layered double hydroxides for oxygen evolution reaction. *Research (Wash D C)* **2020**, 3976278 (2020).
20. M. Ning *et al.*, One-step spontaneous growth of NiFe layered double hydroxide at room temperature for seawater oxygen evolution. *Mater. Today Phys.* **19**, 100419 (2021).
21. Q. Wen *et al.*, Schottky heterojunction nanosheet array achieving high-current-density oxygen evolution for industrial water splitting electrolyzers. *Adv. Energy Mater.* **11**, 2102353 (2021).
22. S. Khatun, P. Roy, Cobalt chromium vanadium layered triple hydroxides as an efficient oxygen electrocatalyst for alkaline seawater splitting. *Chem. Commun. (Camb.)* **58**, 1104–1107 (2022).
23. Y. Hu *et al.*, Constructing a CeO_{2-x}@CoFe-layered double hydroxide heterostructure as an improved electrocatalyst for highly efficient water oxidation. *Inorg. Chem. Front.* **7**, 4461–4468 (2020).
24. L. Wu *et al.*, Boron-modified cobalt iron layered double hydroxides for high efficiency seawater oxidation. *Nano Energy* **83**, 105838 (2021).
25. D. Wang *et al.*, Atomic and electronic modulation of self-supported nickel-vanadium layered double hydroxide to accelerate water splitting kinetics. *Nat. Commun.* **10**, 3899 (2019).
26. P. Li *et al.*, Tuning electronic structure of NiFe layered double hydroxides with vanadium doping toward high efficient electrocatalytic water oxidation. *Adv. Energy Mater.* **8**, 1703341 (2018).
27. L. Wu *et al.*, Facile synthesis of nanoparticle-stacked tungsten-doped nickel iron layered double hydroxide nanosheets for boosting oxygen evolution reaction. *J. Mater. Chem.* **8**, 8096–8103 (2020).
28. X. Zhang *et al.*, Regulation of morphology and electronic structure of FeCoNi layered double hydroxides for highly active and stable water oxidization catalysts. *Adv. Energy Mater.* **11**, 2102141 (2021).
29. K. Zhu *et al.*, Etching-doping sedimentation equilibrium strategy: Accelerating kinetics on hollow Rh-doped CoFe-layered double hydroxides for water splitting. *Adv. Funct. Mater.* **30**, 2003556 (2020).
30. S. Li *et al.*, Ir-O-V catalytic group in Ir-doped $NiV(OH)_2$ for overall water splitting. *ACS Energy Lett.* **4**, 1823–1829 (2019).
31. N. Cheng, L. Ren, X. Xu, Y. Du, S. X. Dou, Recent development of zeolitic imidazolate frameworks (ZIFs) derived porous carbon based materials as electrocatalysts. *Adv. Energy Mater.* **8**, 1801257 (2018).
32. Y. Li *et al.*, Metal-organic frameworks derived interconnected bimetallic metaphosphate nanoarrays for efficient electrocatalytic oxygen evolution. *Adv. Funct. Mater.* **30**, 1910498 (2020).
33. W. Cheng, Z. P. Wu, D. Luan, S. Q. Zang, X. W. D. Lou, Synergetic cobalt-copper-based bimetal-organic framework nanoboxes toward efficient electrochemical oxygen evolution. *Angew. Chem. Int. Ed. Engl.* **60**, 26397–26402 (2021).
34. H. Chen *et al.*, Hierarchical micro-nano sheet arrays of nickel-cobalt double hydroxides for high-rate Ni-Zn batteries. *Adv. Sci. (Weinh.)* **6**, 1802002 (2019).
35. L. Yu *et al.*, Amorphous NiFe layered double hydroxide nanosheets decorated on 3D nickel phosphide nanoarrays: A hierarchical core-shell electrocatalyst for efficient oxygen evolution. *J. Mater. Chem. A Mater. Energy Sustain.* **6**, 13619–13623 (2018).
36. J. Wu *et al.*, Understanding the effect of second metal on CoM (M = Ni, Cu, Zn) metal-organic frameworks for electrocatalytic oxygen evolution reaction. *Small* **17**, e2105150 (2021).
37. F. Song, X. Hu, Exfoliation of layered double hydroxides for enhanced oxygen evolution catalysis. *Nat. Commun.* **5**, 4477 (2014).
38. F. Yang, Y. Chen, G. Cheng, S. Chen, W. Luo, Ultrathin nitrogen-doped carbon coated with CoP for efficient hydrogen evolution. *ACS Catal.* **7**, 3824–3831 (2017).
39. M. Schreier *et al.*, Solar conversion of CO_2 to CO using Earth-abundant electrocatalysts prepared by atomic layer modification of CuO. *Nat. Energy* **2**, 17087 (2017).
40. S. Niu *et al.*, Autogenous growth of hierarchical $NiFe(OH)_x$/FeS nanosheet-on-microsheet arrays for synergistically enhanced high-output water oxidation. *Adv. Funct. Mater.* **29**, 1902180 (2019).
41. C. Liu *et al.*, Amorphous metal-organic framework-dominated nanocomposites with both compositional and structural heterogeneity for oxygen evolution. *Angew. Chem. Int. Ed. Engl.* **59**, 3630–3637 (2020).
42. W. Zhao *et al.*, NiFe layered double hydroxides grown on a corrosion-cell cathode for oxygen evolution electrocatalysis. *Adv. Energy Mater.* **12**, 2102372 (2021).
43. Z. Lu *et al.*, Ternary NiFeMn layered double hydroxides as highly-efficient oxygen evolution catalysts. *Chem. Commun. (Camb.)* **52**, 908–911 (2016).
44. K. Yue *et al.*, In situ ion-exchange preparation and topological transformation of trimetal-organic frameworks for efficient electrocatalytic water oxidation. *Energy Environ. Sci.* **14**, 6546–6553 (2021).
45. H. Han *et al.*, Electronically double-layered metal boride hollow nanoprism as an excellent and robust water oxidation electrocatalysts. *Adv. Energy Mater.* **9**, 1803799 (2019).
46. N. Cheng *et al.*, In-situ grafting of N-doped carbon nanotubes with Ni encapsulation onto MOF-derived hierarchical hybrids for efficient electrocatalytic hydrogen evolution. *Carbon* **163**, 178–185 (2020).
47. X. Xiao *et al.*, Regulating the electronic configuration of ruthenium nanoparticles via coupling cobalt phosphide for hydrogen evolution in alkaline media. *Mater. Today Phys.* **12**, 100182 (2020).
48. L. Yu *et al.*, Ultrafast room-temperature synthesis of porous S-doped Ni/Fe (oxy)hydroxide electrodes for oxygen evolution catalysis in seawater splitting. *Energy Environ. Sci.* **13**, 3439–3446 (2020).
49. L. Yu, Z. Ren, Systematic study of the influence of iR compensation on water electrolysis. *Mater. Today Phys.* **14**, 100253 (2020).
50. S. H. Hsu *et al.*, An earth-abundant catalyst-based seawater photoelectrolysis system with 17.9% solar-to-hydrogen efficiency. *Adv. Mater.* **30**, e1707261 (2018).